

# Accepted Manuscript

Nickel hydroxide/chemical vapor deposition-grown graphene/nickel hydroxide/nickel foam hybrid electrode for high performance supercapacitors

Shude Liu, Ying Yin, Kwan San Hui, Kwun Nam Hui, Su Chan Lee, Seong Chan Jun



PII: S0013-4686(18)32542-8

DOI: <https://doi.org/10.1016/j.electacta.2018.11.070>

Reference: EA 33071

To appear in: *Electrochimica Acta*

Received Date: 9 April 2018

Revised Date: 27 October 2018

Accepted Date: 11 November 2018

Please cite this article as: S. Liu, Y. Yin, K. San Hui, K.N. Hui, S.C. Lee, S. Chan Jun, Nickel hydroxide/chemical vapor deposition-grown graphene/nickel hydroxide/nickel foam hybrid electrode for high performance supercapacitors, *Electrochimica Acta* (2018), doi: <https://doi.org/10.1016/j.electacta.2018.11.070>.

This is a PDF file of an unedited manuscript that has been accepted for publication. As a service to our customers we are providing this early version of the manuscript. The manuscript will undergo copyediting, typesetting, and review of the resulting proof before it is published in its final form. Please note that during the production process errors may be discovered which could affect the content, and all legal disclaimers that apply to the journal pertain.

**Nickel hydroxide/chemical vapor deposition-grown graphene/nickel hydroxide/nickel foam hybrid electrode for high performance supercapacitors**

Shude Liu <sup>a</sup>, Ying Yin <sup>a,b</sup>, Kwan San Hui <sup>c</sup>, Kwun Nam Hui <sup>\*,d</sup>, Su Chan Lee <sup>a</sup>, Seong Chan Jun <sup>\*,a</sup>

<sup>a</sup>School of Mechanical Engineering, Yonsei University, Seoul 120-749, South Korea.

<sup>b</sup>Guangxi Key Laboratory of Information Materials, Guilin University of Electronic Technology, Guilin, P. R. China.

<sup>c</sup>Faculty of Science and Engineering, University of East Anglia, Norwich NR47TJ, UK.

<sup>d</sup>Institute of Applied Physics and Materials Engineering, University of Macau, Avenida da Universidade, Taipa, Macau, China.

\* E-mail: scj@yonsei.ac.kr (Seong Chan Jun)

Email: bizhui@umac.mo (Kwun Nam Hui)

**Keywords:** CVD-grown graphene, nickel hydroxide, hybrid electrode, electrochemical performance, supercapacitors

**Abstract**

Rational design of electrode structures has been recognized as an effective strategy to improve the electrochemical performance of electrode materials. Herein, we demonstrate an integrated electrode in which nickel hydroxide (Ni(OH)<sub>2</sub>) nanosheets are deposited on both sides of chemical vapor deposition-grown graphene on Ni foam, which not only effectively optimizes electrical conductivity of Ni(OH)<sub>2</sub>, but also accommodates the structural deformation associated with the large volume change

upon cycling. The synthesized Ni(OH)<sub>2</sub>/graphene/Ni(OH)<sub>2</sub>/Ni foam electrode exhibits a high specific capacity of 991 C g<sup>-1</sup> at a current density of 1 A g<sup>-1</sup>, which is higher than the theoretical specific capacity of additive sum of Ni(OH)<sub>2</sub> and graphene, and retains 95.4% of the initial capacity after 5000 cycles. A hybrid supercapacitor is constructed by using Ni(OH)<sub>2</sub>/graphene/Ni(OH)<sub>2</sub>/Ni foam as the positive electrode and activated carbon on Ni foam as the negative electrode, which achieves a maximum energy density of 49.5 W h kg<sup>-1</sup> at a power density of 750 W kg<sup>-1</sup>, and excellent cycling lifespans with 89.3% retention after 10000 cycles at 10 A g<sup>-1</sup>.

## 1 Introduction

Increasing efforts are currently being devoted toward developing superior electrochemical supercapacitors in view of their higher power density, better cycling stability, and faster charge/discharge characteristic than secondary batteries, while higher energy density compared to conventional dielectric capacitors [1-3]. Battery-type materials of transition metal oxides have been extensively studied as they can provide dominant high specific capacity by fast and reversible faradaic redox reactions [4, 5]. Among these, nickel hydroxide (Ni(OH)<sub>2</sub>) has been considered as a potential material for supercapacitors owing to its high theoretical specific capacity, highly reversible redox activity, natural abundance, stability in alkaline media, and layered structure for favorable ion diffusion [6, 7]. Unfortunately, Ni(OH)<sub>2</sub>-based electrode materials still suffer from low specific capacity, rapid capability fading, and inferior cycling stability due to their intrinsically poor conductivity and unstable

geometric structures [8], thereby impeding their practical applications. Therefore, the development of Ni(OH)<sub>2</sub>-based electrodes with excellent electrochemical performances remains a pressing topic in supercapacitor technology development.

Accordingly, effective strategies have been proposed to boost the electrochemical performance of Ni(OH)<sub>2</sub> by engineering electrode designs and optimizing the electrical properties of materials [9, 10]. Salunkhe et al. reported coaxial growth of Ni(OH)<sub>2</sub> on a highly conductive CNT backbone, which resulted in enhanced electrical conductivity and increased electrochemically active sites, resulting in highly improved electrochemical performance [8]. Yan et al. reported hierarchical Ni(OH)<sub>2</sub> nanoflakes anchored on rGO nanosheets. The produced hybrid architectures shortened the electrolyte ion diffusion path and created numerous macropores that acted as ion-buffering reservoirs to sustain the Faradaic reactions at a high current density [11]. Wang et al. synthesized Ni(OH)<sub>2</sub> nanosheets on a nickel conducting substrate, exhibiting an ultrahigh specific capacity of 790.3 C g<sup>-1</sup> at a current density of 5 mA cm<sup>-2</sup>. This was attributed to the structural robustness and rapid electron transport of the integrated electrode [12]. Despite attaining enhanced electrochemical performances in some cases, most of these currently available reported composites simply level off the electroactive species, which is then accompanied by low degrees of exposed edge sites, slow reaction kinetics, and poor structural integrity. This usually results in a limited specific capacity and cycle stability to some degree. Compared to the chemically synthesized rGO, graphene prepared by chemical vapor

deposition (CVD) offers better conductive properties owing to their large crystal domains and fewer defects in the graphene layers [13, 14]. However, it is very challenging to grow CVD graphene on transition metal oxides and hydroxides due to the harsh CVD graphene growth mechanism.

In this work, we develop a new synthetic approach to realize a 3D integrated Ni(OH)<sub>2</sub>/CVD-grown graphene (G)/Ni(OH)<sub>2</sub>/Ni foam (NF) hybrid electrode, in which a fracture in the CVD graphene is intentionally created by sonication, followed by a subsequent hydrothermal growth of Ni(OH)<sub>2</sub> nanosheets on NF. Owing to the well-defined electrochemical properties of Ni(OH)<sub>2</sub>, and the highly conductive behavior and structural robustness of graphene and porous NF substrate, the integrated Ni(OH)<sub>2</sub>/G/Ni(OH)<sub>2</sub>/NF electrode exhibits a high specific capacity of 991 C g<sup>-1</sup> at a current density of 1 A g<sup>-1</sup>, and remains 677 C g<sup>-1</sup> even at 20 A g<sup>-1</sup>. A hybrid supercapacitor device composed of the as-fabricated Ni(OH)<sub>2</sub>/G/Ni(OH)<sub>2</sub>/NF and AC/NF delivers a maximum energy density of 49.5 W h kg<sup>-1</sup> at a power density of 750 W kg<sup>-1</sup>, and maximum power density of 7500 W kg<sup>-1</sup> can be retained with an energy density of 26.9 W h kg<sup>-1</sup>.

## 2 Experimental details

**2.1 Synthesis of graphene on nickel foam (G/NF).** The G/NF was prepared by a modified CVD procedure [15]. Specifically, the NFs were placed in a CVD tube furnace under H<sub>2</sub> (5 sccm) atmosphere and maintained for 45 min at 1000 °C to

eliminate any oil contamination and remove the oxide layer from the surface. Afterwards, CH<sub>4</sub> gas was continuously introduced into the tube at a constant pressure (55 mTorr). After 45 min under this reaction-gas mixture flow, the furnace was rapidly cooled to ambient temperature under a protective H<sub>2</sub> atmosphere (5 sccm) at a rate of ~20 °C min<sup>-1</sup>.

**2.2 Synthesis of Ni(OH)<sub>2</sub>/G/Ni(OH)<sub>2</sub>/NF hybrid electrode.** Prior to the experiment, fractures (several micrometers in size) on G/NF were generated by ultrasonic treatment of the G/NF in distilled water for 12 h, in which the strong mechanical vibrations induced regional fractures on the graphene. In addition, the intercalation of dissolved oxygen from the distilled water can cause a wicking effect between CVD graphene and NF [16, 17], which effectively delaminated CVD graphene from the NF substrate. Typically, 2 mmol of Ni(NO<sub>3</sub>)<sub>2</sub>·6H<sub>2</sub>O, 4 mmol of NH<sub>4</sub>F, and 12 mmol of CO(NH<sub>2</sub>)<sub>2</sub> were dissolved in 60 mL of distilled water under vigorous stirring. The above solution, containing the pretreated G/NF substrate, was kept for 6 h at room temperature to ensure that the precursor particles could fully penetrate into the internal intercalation of G/NF, which was then transferred to a 50 mL autoclave and maintained at 110 °C for 6 h. After the autoclave cooled down naturally to room temperature, the precipitate-covered G/NF was removed, washed with deionized water and ethanol, and then dried at 70 °C for 12 h. Finally, the Ni(OH)<sub>2</sub>/G/Ni(OH)<sub>2</sub>/NF hybrid electrode was obtained. As a reference, Ni(OH)<sub>2</sub>/NF and Ni(OH)<sub>2</sub>/G/NF were also fabricated using the same hydrothermal process, but without the ultrasonic treatment, leading to directly deposited Ni(OH)<sub>2</sub> onto the

surface of G/NF and NF substrates.

**2.3 Material characterization.** Field-emission scanning electron microscopy (FE-SEM, JSM7800F, JEOL) and transmission electron microscopy (TEM, JEM-2100, JEOL) equipped with energy-dispersive X-ray spectroscopy (EDS) were employed to analyze the morphologies and structural features of the composites. Focused ion beam scanning electron microscopy (FIB-SEM) was conducted using a Dual Beam Strata 235 (FEI) and Auriga Compact (Zeiss) microscope. X-ray diffraction (XRD) patterns were collected using a Philips 1710 diffractometer with Cu-K $\alpha$  radiation ( $k = 1.5418 \text{ \AA}$ ). Raman spectra (LabRAM Aramis, Horiba Jobin Yvon) were recorded using a conventional backscattering geometry and liquid-nitrogen-cooled charge-coupled device multichannel detector. X-ray photoelectron spectroscopy (XPS) was performed using an Escalab220 K-alpha spectrometer (Thermo Scientific, UK).

**2.4 Electrochemical measurements.** Electrochemical measurements were carried out using a multichannel electrochemical workstation (nSTAT, Ivium Technologies). A three-electrode single compartment cell was used in a 1 M KOH electrolyte. The mass loadings of the active materials weighted before and after pristine NF substrate for G/NF, Ni(OH) $_2$ /NF, Ni(OH) $_2$ /G/NF, and Ni(OH) $_2$ /G/Ni(OH) $_2$ /NF were approximately 0.2, 1.8, 1.6, and 1.5 mg cm $^{-2}$ , respectively. The as-fabricated electrodes were directly used as the working electrode ( $1 \times 1 \text{ cm}^{-2}$ ), while a saturated calomel electrode and platinum foil served as the reference electrode and counter electrode, respectively. Electrochemical impedance spectroscopy (EIS) measurements were recorded in the frequency range from 100 kHz to 0.01 Hz at the open circuit potential with an oscillation amplitude of 5 mV. The specific capacity ( $C_s$ , C g $^{-1}$ ) of the electrode materials was calculated from the discharge curves using the equation  $C_s = (I \times \Delta t) / m$

[6], where  $m$  (g) is the mass of the active materials,  $I$  (A) is the discharge current, and  $\Delta t$  (s) is the discharge time.

The theoretical faradaic capacity  $C_1$  ( $C\ g^{-1}$ ) of  $Ni(OH)_2$  was calculated using Faraday's law  $C_1 = n \times F / (1000 \times M_w)$  [18], where  $n$  is the moles of the charge transferred per mole of active material,  $F$  is the Faraday constant ( $96485.3\ C\ mol^{-1}$ ), and  $M_w$  ( $kg\ mol^{-1}$ ) is the molar mass of the active material. For  $Ni(OH)_2$ ,  $n$  is one mole of electron transfer and  $M_w$  of  $Ni(OH)_2$  is  $92.7 \times 10^{-3}\ kg\ mol^{-1}$ ; thus, the theoretical faradaic capacity was calculated to be about  $1040.8\ C\ g^{-1}$ .

According to the theory of quantum capacitance of ideal graphene proposed by Xia et al. [19], the theoretical quantum capacitance  $C_2$  ( $F\ g^{-1}$ ) of ideal graphene was calculated to be  $\sim 550\ F\ g^{-1}$  when the entire surface area can be fully utilized. In our prepared system, the working potential of GCD process ranges from 0 to 0.45 vs. SCE/V. The corresponding theoretical specific capacity  $C_3$  ( $C\ g^{-1}$ ) of ideal graphene is calculated as follow:  $C_3 = C_2 \times \text{potential window} = 550 \times 0.45\ C\ g^{-1} = 247.5\ C\ g^{-1}$ .

The mass loadings of  $Ni(OH)_2/G/Ni(OH)_2/NF$  and  $G/NF$  weighted before and after pristine NF substrate is  $\sim 1.5$  and  $\sim 0.2\ mg\ cm^{-2}$ , respectively. Accordingly, the mass ratios of  $Ni(OH)_2$  and graphene to  $Ni(OH)_2/G/Ni(OH)_2/NF$  are  $\frac{1.5-0.2}{1.5} \times 100\%$  and  $\frac{0.2}{1.5} \times 100\%$ , respectively. Based on the discussion above, the theoretical faradaic capacity ( $C\ g^{-1}$ ) of additive sum of  $Ni(OH)_2$  and graphene is  $1040.8\ C\ g^{-1} \times \frac{1.3}{1.5} + 247.5\ C\ g^{-1} \times \frac{0.2}{1.5} \approx 935\ C\ g^{-1}$ .

Prior to the assembly of a hybrid supercapacitor, the negative electrode was prepared by mixing activated carbon (AC) and polytetrafluoroethylene at a weight ratio of 95:5,

and then spread on a piece of NF (area =  $1 \times 1 \text{ cm}^2$ ). A hybrid device using the  $\text{Ni}(\text{OH})_2/\text{G}/\text{Ni}(\text{OH})_2/\text{NF}$  as the positive electrode and  $\text{AC}/\text{NF}$  as the negative electrode was assembled together with one layer of cellulose paper as the separator using 1 M KOH electrolyte. Because the constructed hybrid supercapacitor delivered quasi-rectangular CV curves, the specific capacitance  $C_h$  ( $\text{F g}^{-1}$ ) of the hybrid supercapacitor was calculated using  $(I \cdot \Delta t)/(M \cdot \Delta V)$  [20], where  $M$  (mg) is the total mass of the active materials in the device. The energy density  $E$  ( $\text{W h kg}^{-1}$ ) and power density  $P$  ( $\text{W kg}^{-1}$ ) of the hybrid device was calculated by  $E = C_h \cdot \Delta V^2/7.2$  and  $P = 3600 \cdot E/\Delta t$  [21], where  $\Delta V$  represents the discharging cell potential range (V).

### 3 Results and discussion

The synthesis procedure of  $\text{Ni}(\text{OH})_2/\text{G}/\text{Ni}(\text{OH})_2/\text{NF}$  integrated architecture is illustrated in Fig. 1. Graphene is first deposited on the surface of 3D interconnected porous Ni foam through CVD, followed by ultrasonic treatment to force the delamination of regional fractures in CVD graphene from the NF substrate. Then, the as-obtained G/NF is selected as a template to grow  $\text{Ni}(\text{OH})_2$  via a hydrothermal process, forming  $\text{Ni}(\text{OH})_2$  nanosheets distribute on both sides of CVD graphene grown on NF. For the preparation of  $\text{Ni}(\text{OH})_2/\text{NF}$  and  $\text{Ni}(\text{OH})_2/\text{G}/\text{NF}$  samples,  $\text{Ni}(\text{OH})_2$  nanosheets are separately anchored on NF and G/NF template without pre-ultrasonic treatment by the same hydrothermal condition.

An XRD study was performed to analyze the crystallographic structure of the as-prepared  $\text{Ni}(\text{OH})_2/\text{NF}$ ,  $\text{Ni}(\text{OH})_2/\text{G}/\text{NF}$ , and  $\text{Ni}(\text{OH})_2/\text{G}/\text{Ni}(\text{OH})_2/\text{NF}$  (Fig. 2a). The XRD pattern of  $\text{Ni}(\text{OH})_2/\text{NF}$  reveals three strong diffraction peaks at the  $2\theta$  values of

44.8°, 51.9°, and 76.6°, which match well with those of the nickel substrate (JCPDS No. 70-0989) [22]. The diffraction peaks at 19.0°, 33.2°, 38.6°, and 59.4° are assigned to the (001), (100), (101), and (110) reflections of the hexagonal  $\beta$ -Ni(OH)<sub>2</sub> phase (JCPDS No. 01-1047) [23]. In contrast, Ni(OH)<sub>2</sub>/G/Ni(OH)<sub>2</sub>/NF and Ni(OH)<sub>2</sub>/G/NF show two additional diffraction peaks at 26.5° and 54.5°, which are identified as the (002) and (004) planes of graphitic carbon (JCPDS No. 75-1621), respectively [24]. The peak corresponding to the graphitic carbon phase of Ni(OH)<sub>2</sub>/G/Ni(OH)<sub>2</sub>/NF appears with a relatively stronger intensity in comparison to that of Ni(OH)<sub>2</sub>/G/NF, which might derive from the encapsulation of Ni(OH)<sub>2</sub> by the CVD graphene layer. The survey spectrum of G/NF shows the existence of carbon, oxygen, and nickel species (Fig. 2b). The Raman spectra of Ni(OH)<sub>2</sub>/NF, Ni(OH)<sub>2</sub>/G/NF, and Ni(OH)<sub>2</sub>/G/Ni(OH)<sub>2</sub>/NF exhibits characteristic peaks located at 463, 3576, and 3643 cm<sup>-1</sup>, corresponding to the symmetric Ni–OH stretching mode, symmetric stretching of the hydroxyl groups, and O–H vibration of the hydrogen-bonded hydroxyl groups derived from the water molecules in the interlamellar space of Ni(OH)<sub>2</sub>, respectively [25-27]. In the Raman spectra of G/NF, Ni(OH)<sub>2</sub>/G/NF, and Ni(OH)<sub>2</sub>/G/Ni(OH)<sub>2</sub>/NF, two prominent G and 2D bands are observed at 1585 and 2712 cm<sup>-1</sup>, which can be attributed to the characteristic peaks of CVD graphene [24]. The D-mode located at 1357 cm<sup>-1</sup> also appears in the spectra of Ni(OH)<sub>2</sub>/G/Ni(OH)<sub>2</sub>/NF and Ni(OH)<sub>2</sub>/G/NF, confirming that structural defects are produced.

XPS analysis was performed to examine the chemical composition and chemical state of the samples. The survey spectra of Ni(OH)<sub>2</sub>/NF, Ni(OH)<sub>2</sub>/G/NF, and Ni(OH)<sub>2</sub>/G/Ni(OH)<sub>2</sub>/NF mainly shows the presence of Ni, O, and C species (Fig. S1). An additional weak F 1s peak is observed at 685.3 eV, which provides evidence for fluoride ions of NH<sub>4</sub>F being intercalated into the interlamellar space of Ni(OH)<sub>2</sub>. The lower binding energy peak in the deconvoluted O 1s spectrum, locates at 531.3 eV, corresponds to the formation of metal hydroxide (Ni–O–H) [28], whereas the other peak at 532.5 eV can be indexed to the physisorbed and chemisorbed water near the surface (Fig. 2c) [29]. The high-resolution Ni 2p core level XPS spectra reveals the two major peaks of Ni 2p<sub>1/2</sub> and Ni 2p<sub>3/2</sub>, centered at 873.5 and 855.9 eV, respectively, together with two shakeup satellites located at 879.7 and 862.1 eV (Fig. 2d) [6, 21]. The spin-energy separation of approximately 17.6 eV between the two major peaks can be ascribed to the characteristic Ni(OH)<sub>2</sub> phase, which agrees with the previous reports [30, 31].

FE-SEM images show CVD-grown graphene grown on NF (Fig. S2a–d) and the corresponding fractures (Fig. S2e–f) obtained from the intended sonication. Wrinkle-like graphene with irregular fractures is found to fully cover the NF skeleton. SEM images of Ni(OH)<sub>2</sub>/NF show that the Ni(OH)<sub>2</sub> nanosheets are uniformly supported on the NF substrate to provide a conformal coating on its surface (Fig. S3). The enlarged SEM image shows how the Ni(OH)<sub>2</sub> nanosheets are homogeneously aligned and interconnected with each other, forming a unique nanoarray with highly

open features, which is conducive to providing pathways for effective ion transport. In comparison to Ni(OH)<sub>2</sub>/NF, the overall morphology of Ni(OH)<sub>2</sub>/G/NF remains unchanged except for the active materials grown on the skeleton of G/NF (Fig. S4). TEM observations reveal that individual nanosheets possess a hexagonal shape with an angle of around 120° in the adjacent edge (Fig. S5a). A high resolution TEM image shows that the lattice fringe has a spacing distance of 0.270 nm and corresponds to the (100) lattice spacing of Ni(OH)<sub>2</sub> (Fig. S5b). The regular hexagonal pattern observed in the selected area electron diffraction (SAED) indicates the monocrystalline feature of the Ni(OH)<sub>2</sub> nanosheets (Fig. S5c). The Ni(OH)<sub>2</sub>/G/Ni(OH)<sub>2</sub>/NF exhibits that the Ni(OH)<sub>2</sub> nanosheets are uniformly embedded in the interlayer between graphene and NF in addition to the flower-like Ni(OH)<sub>2</sub> depositing on the surface of CVD-grown graphene (Fig. 3a-d). The structure of Ni(OH)<sub>2</sub>/G/Ni(OH)<sub>2</sub>/NF is further investigated by tomographic analysis using FIB–SEM and TEM. Fig. 3e reveals that Ni(OH)<sub>2</sub> nanosheets lying perpendicular to the NF substrate while being encapsulated by the CVD graphene layers. The high resolution TEM image of the embedded Ni(OH)<sub>2</sub> reveals a lattice fringe with a spacing of 0.270 nm (Fig. 3f), which matches well with the (100) plane of the hexagonal Ni(OH)<sub>2</sub> phase, in agreement with the XRD results.

The electrochemical behavior of the synthesized samples was investigated in a 1 M KOH aqueous electrolyte using a three-electrode configuration. Fig. 4a shows the cyclic voltammetry (CV) curves of the Ni(OH)<sub>2</sub>/NF, Ni(OH)<sub>2</sub>/G/NF, and Ni(OH)<sub>2</sub>/G/Ni(OH)<sub>2</sub>/NF electrodes at a scan rate of 30 mV s<sup>-1</sup> over a potential range from 0 to 0.5 vs. SCE/V. A pair of well-defined redox peaks is visible in the CV

curves of the as-synthesized electrodes, which can be indexed to the well-documented  $\text{Ni}^{2+}/\text{Ni}^{3+}$  [6], suggesting that the charge storage mainly stems from the Faradaic reaction of the redox-active  $\text{Ni}(\text{OH})_2$  instead of a double-layer process from the CVD graphene layers. Evidently, the integral area surrounded by the CV curve significantly increases with the introduction of the enclosed CVD graphene on  $\text{Ni}(\text{OH})_2/\text{NF}$ . As shown in Fig. S6, the integrated area of G/NF is quite small relative to that of the other electrodes (about 1.8% capacity of the  $\text{Ni}(\text{OH})_2/\text{G}/\text{Ni}(\text{OH})_2/\text{NF}$  electrode), indicating that the capacity contribution from the G/NF can be negligible. To further evaluate the electrochemical performances of  $\text{Ni}(\text{OH})_2/\text{NF}$ ,  $\text{Ni}(\text{OH})_2/\text{G}/\text{NF}$ , and  $\text{Ni}(\text{OH})_2/\text{G}/\text{Ni}(\text{OH})_2/\text{NF}$ , the CV curves were measured at various scan rates between 5 to  $50 \text{ mV s}^{-1}$  (Fig. S7). It is worthy to note that a pair of broad redox peaks with oxidation peak at  $\sim 0.32 \text{ vs. SCE/V}$  and a reduction peak at  $\sim 0.28 \text{ vs. SCE/V}$  is observed in CV curves of as-synthesized samples at a low scan rate of  $5 \text{ mV s}^{-1}$ , which is attributed to the reversible intercalation/deintercalation of electrolyte ions in the inter-sheet spacing of the layered  $\text{Ni}(\text{OH})_2$  [32]. To further investigate the charge storage mechanism of  $\text{Ni}(\text{OH})_2/\text{G}/\text{Ni}(\text{OH})_2/\text{NF}$ , the relationship between cathodic current responds ( $I_p$ ) from CV curves and the scan rate ( $\nu$ ) is analyzed using a power-law ( $I_p = a \times \nu^b$ ) [33]. Where  $b = 1$  indicates that the reaction is surface-controlled, while  $b = 0.5$  represents that the reaction is diffusion-controlled process. The obtained  $b$ -value of the  $\text{Ni}(\text{OH})_2/\text{G}/\text{Ni}(\text{OH})_2/\text{NF}$  electrodes is 0.58 (Fig. S8), which is close to 0.5, indicating a dominated diffusion-controlled process. To determine quantitatively the Faradaic contribution to the total charge, the cathodic

current response ( $i$ ) at a fixed potential window ( $V$ ) could be separated as two parts according to the equation of  $i(V) = k_1V + k_2V^{1/2}$  [34], where the terms  $k_1V$  and  $k_2V^{1/2}$  correspond to the charge contributed from capacitive and diffusion-controlled faradaic processes, respectively. It can be found that the charge storage attributed by the Faradaic process for Ni(OH)<sub>2</sub>/G/Ni(OH)<sub>2</sub>/NF electrode decreases with increasing scan rate from 90.8% at 5 mV s<sup>-1</sup> to 76.2% at 50 mV s<sup>-1</sup> (Fig. 4b). The results indicate the relatively high contribution of the Faradaic process to the total stored charge.

Fig. 4c shows the nonlinear characteristics of the galvanostatic charge/discharge (GCD) curves of the Ni(OH)<sub>2</sub>/NF, Ni(OH)<sub>2</sub>/G/NF, and Ni(OH)<sub>2</sub>/G/Ni(OH)<sub>2</sub>/NF electrodes at a current density of 1 A g<sup>-1</sup>, implying these materials demonstrated the typical Faradaic behavior of battery-type electrodes [35, 36]. The discharge curves of the electrodes are almost symmetric to the corresponding charge curves at various current densities, implying good reaction reversibility. Clearly, as indicated by the CV results, the Ni(OH)<sub>2</sub>/G/Ni(OH)<sub>2</sub>/NF presents a longer discharging time than Ni(OH)<sub>2</sub>/NF and Ni(OH)<sub>2</sub>/G/NF. The specific capacity calculated from the discharge curves is shown in Fig. 4d. The Ni(OH)<sub>2</sub>/G/Ni(OH)<sub>2</sub>/NF electrode achieves the highest specific capacity of 991 C g<sup>-1</sup> at a current density of 1 A g<sup>-1</sup>, which is beyond the theoretical capacity (935 C g<sup>-1</sup>) of additive sum of Ni(OH)<sub>2</sub> and graphene (details in experiment section). The ultrahigh specific capacity of the Ni(OH)<sub>2</sub>/G/Ni(OH)<sub>2</sub>/NF electrode is ascribed to the nearly full redox reaction and additional electrical double-layer capacitance provided by Ni(OH)<sub>2</sub> nanostructure and the raised

capacitance contribution caused by the inevitable defects in graphene nanostructure [37, 38]. The specific capacity value of  $\text{Ni(OH)}_2/\text{G}/\text{Ni(OH)}_2/\text{NF}$  is nearly 2.30 and 1.35 times higher than that of  $\text{Ni(OH)}_2/\text{NF}$  ( $430 \text{ C g}^{-1}$ ) and  $\text{Ni(OH)}_2/\text{G}/\text{NF}$  ( $738 \text{ C g}^{-1}$ ), respectively. More importantly, the  $\text{Ni(OH)}_2/\text{G}/\text{Ni(OH)}_2/\text{NF}$  electrode still exhibits about 70.7% retention of its initial capacity upon increasing the current density from 1 to  $20 \text{ A g}^{-1}$ , which is higher than that of  $\text{Ni(OH)}_2/\text{G}/\text{NF}$  (~60.9%) and  $\text{Ni(OH)}_2/\text{NF}$  (~62.6%). The rate capability of  $\text{Ni(OH)}_2/\text{G}/\text{Ni(OH)}_2/\text{NF}$  is also highly competitive compared to most of the previously reported carbon/ $\text{Ni(OH)}_2$  systems (Table S1) [8, 39-43].

The cycle life stability of  $\text{Ni(OH)}_2/\text{NF}$ ,  $\text{Ni(OH)}_2/\text{G}/\text{NF}$ , and  $\text{Ni(OH)}_2/\text{G}/\text{Ni(OH)}_2/\text{NF}$  was measured at a high current density of  $20 \text{ A g}^{-1}$ , as shown in Fig. 4e.  $\text{Ni(OH)}_2/\text{NF}$  shows a 81.1% capacity retention after 5000 cycles, while the  $\text{Ni(OH)}_2/\text{G}/\text{NF}$  electrode exhibits a highly improved capacity retention rate (90.3%) after the long-term test, revealing its excellent cycling behavior. This is attributed to the high electrical conductivity of the G/NF substrate. In contrast, the specific capacity of  $\text{Ni(OH)}_2/\text{G}/\text{Ni(OH)}_2/\text{NF}$  increases at first because of the uncompleted activation of the electrochemical active materials, resulting in an increased mobility of the surface charge and electrolyte transfer [44]; however, it then gradually degrades to a stabilized level at approximately 95.4% of the initial capacity, even after the same cycling test. Such cyclic stability is significantly higher than that of  $\text{Ni(OH)}_2$ -derived hybrid materials (Table S2) [31, 45-47], verifying the significance of the

Ni(OH)<sub>2</sub>/G/Ni(OH)<sub>2</sub>/NF architecture. Importantly, the as-synthesized electrodes retain a high Coulombic efficiency of over 96%, even after 5000 cycles (Fig. S9), indicating their superior ability to retain charge during the long-term cycling test. SEM images (Fig. S10) of the Ni(OH)<sub>2</sub>/G/Ni(OH)<sub>2</sub>/NF electrode show a slight aggregation of the Ni(OH)<sub>2</sub> nanosheets after the cycling test, which accounts for the remarkable cycling stability. To further investigate the electrochemical behaviors of Ni(OH)<sub>2</sub>/NF, Ni(OH)<sub>2</sub>/G/NF and Ni(OH)<sub>2</sub>/G/Ni(OH)<sub>2</sub>/NF, EIS measurements were carried out. A suppressed semicircle at a high frequency region and a sloped line at a low frequency region for all the impedance plots can be observed (Fig. S11). An equivalent circuit is proposed based on the following elements: the equivalent series resistance ( $R_s$ ), which is a combination of the electrolyte resistance, the intrinsic resistance, and the contact resistance between electroactive material and current collector [48]. The charge transfer resistance ( $R_{ct}$ ) corresponds to the charge transfer resistance at the electrode/electrolyte interface [49]. Taking into account that the porous feature of as-synthesized electrode materials causes the part of the electrochemical process that deviates from the nature of the pure capacitance, a constant phase element (CPE) is introduced to fit the EIS measurement. CPE presents the inhomogeneity of the electrode surface and inhomogeneity of the charge distribution associated with electrode geometry in the EIS measurement [50-52]. The interface capacitance could be expected in parallel with  $R_{ct}$ , and Warburg diffusion element ( $Z_w$ ) corresponding to the ion diffusion [53, 54]. Moreover, the capacitive nature could be reasonably presented as CPE in parallel with  $R_{ct}$  [55]. The fitted parameter values are listed in

Table S3 for comparison. The  $R_s$  values of Ni(OH)<sub>2</sub>/NF, Ni(OH)<sub>2</sub>/G/NF, and Ni(OH)<sub>2</sub>/G/Ni(OH)<sub>2</sub>/NF are 1.19, 0.84, and 0.63  $\Omega$ , respectively, suggesting their low internal resistant. Compared to Ni(OH)<sub>2</sub>/NF (~17.13  $\Omega$ ) and Ni(OH)<sub>2</sub>/G/NF (~10.07  $\Omega$ ), Ni(OH)<sub>2</sub>/G/Ni(OH)<sub>2</sub>/NF possesses a smaller  $R_{ct}$  value (~2.31  $\Omega$ ), indicating faster charge transport properties. The  $Z_w$  of the Ni(OH)<sub>2</sub>/NF, Ni(OH)<sub>2</sub>/G/NF, and Ni(OH)<sub>2</sub>/G/Ni(OH)<sub>2</sub>/NF are determined to be 2.83, 2.54, and 1.95  $\Omega s^{1/2}$ , respectively. The lower  $Z_w$  value of Ni(OH)<sub>2</sub>/G/Ni(OH)<sub>2</sub>/NF demonstrates better diffusion rate of electrolyte ions within the typical sample [48]. It can be observed that the EIS plot of Ni(OH)<sub>2</sub>/G/Ni(OH)<sub>2</sub>/NF shows a larger slope compared with those of Ni(OH)<sub>2</sub>/G/NF and Ni(OH)<sub>2</sub>/NF at the low frequency region, which indicates better capacitive nature [48]. The results can be explained from the structural merits of the Ni(OH)<sub>2</sub>/G/Ni(OH)<sub>2</sub>/NF electrode: (1) high conductivity of the CVD graphene enhances the electric conductivity of the matrix, resulting in high capacity and rate performance; (2) high mechanical durability of CVD graphene acts as a protective shell to remit the structural deterioration of the Ni(OH)<sub>2</sub> nanostructure, leading to remarkable cycling stability; (3) the steady adhesion of the active materials Ni(OH)<sub>2</sub> on the conductive substrate creates an express path for fast electron transport, and avoids the “dead volume” and “dead weight” in electrode materials typically associated with binders and conductive agents.

To further investigate the Ni(OH)<sub>2</sub>/G/Ni(OH)<sub>2</sub>/NF electrode for practical application, a hybrid supercapacitor was assembled based on Ni(OH)<sub>2</sub>/G/Ni(OH)<sub>2</sub>/NF as the

positive electrode and AC/NF as the negative electrode (Fig. S12) by using 1 M KOH as the electrolyte and cellulose paper as the separator (Fig. 5a). The fabricated hybrid supercapacitor is operated in a two-electrode configuration. The capacitive performance of AC/NF is investigated using CV and GCD measurements within a potential window from  $-1$  to  $0$  vs. SCE/V, as shown in Fig. S13. The CV curves are nearly rectangular and symmetric in shape, even though the scan rate is extended from  $5$  to  $50$   $\text{mV s}^{-1}$  (Fig. S13a), suggesting ideal capacitive properties together with high reversibility [8]. The specific capacitance is calculated from the GCD curves, as illustrated in Fig. S13b–c. The AC/NF electrode presents a specific capacitance of  $224.6$   $\text{F g}^{-1}$  at a current density of  $1$   $\text{A g}^{-1}$ , and retains a capacitance of up to  $118.2$   $\text{F g}^{-1}$ , even at the high current density of  $10$   $\text{A g}^{-1}$ . The impressive capacitive behavior of the AC/NF electrode makes it suitable as a negative electrode. In order to obtain the optimized electrochemical performance, the mass ratio of the positive to negative materials is set to  $0.21$  in the assembled  $\text{Ni}(\text{OH})_2/\text{G}/\text{Ni}(\text{OH})_2/\text{NF}//\text{AC}/\text{NF}$  hybrid device according to the specific capacitance calculated from their CV curves (Fig. 5b) by using the charge balance theory [56]. Fig. 5c shows the CV curves of the fabricated device at a constant scan rate of  $10$   $\text{mV s}^{-1}$  within different cell potentials. As expected, the stable electrochemical window of the hybrid device can be extended to  $1.5$  V. Fig. 5d shows the CV curves recorded at different scan rates. The CV curves show a quasi-rectangular shape with two broad reversible redox peaks, which indicate that the capacitance is derived from the combined contribution of electrochemical double-layer capacitance of AC and the redox reaction associated with  $\text{Ni}^{2+}/\text{Ni}^{3+}$ .

Upon variation of the scan rate from 10 to 50  $\text{mV s}^{-1}$ , the shapes of the CV curves show no obvious diminishing area, implying a fast I-V response and reversible electrochemical behavior [56].

The nearly symmetric charge-discharge curves, with a slight internal cell potential drop, indicate a high reversibility and small internal resistance (Fig. 5e) [35, 57]. It is worth mentioning that the GCD curves recorded at high current density exhibit a more reasonable symmetry, which can be attributed to a higher ratio of the irreversible process (after the redox peaks) in the positive current region at low current density than that at high current density [35]. The specific capacitance of the hybrid device is calculated based on the total mass of the active materials, as shown in Fig. 5f. The specific capacitance could reach  $158.5 \text{ F g}^{-1}$  when the current density is  $1 \text{ A g}^{-1}$ , while remaining at  $86.0 \text{ F g}^{-1}$  at a high current density of  $10 \text{ A g}^{-1}$ , indicating a high rate capability. The long-term cycle stability was evaluated after 10000 continuous GCD cycles at a current density of  $10 \text{ A g}^{-1}$  (Fig. 5g). Almost 89.3% of the initial specific capacitance remains after the cycling test, suggesting excellent cycle stability. To evaluate the potential of the  $\text{Ni}(\text{OH})_2/\text{G}/\text{Ni}(\text{OH})_2/\text{NF}$  electrode architecture in practical applications, such as electrical vehicles, the energy efficiency ( $\eta_E$ ) is investigated as a critical parameter (Fig. S14). Energy efficiency can be obtained from the equation  $\eta_E = E_D/E_C$  [35], where  $E_C$  and  $E_D$  are the charge energies from the charge and discharge curves, respectively. The energy efficiency is found to be nearly 91.8% in the initial cycles and decreases slightly to 86.3% after the cycling test.

A Ragone plot (energy density vs. power density) is used as a performance indicator for practical applications. It is found that the hybrid device delivers a maximum specific energy of  $49.5 \text{ W h kg}^{-1}$  at a specific power of  $750 \text{ W kg}^{-1}$ , while the maximum specific power of  $7500 \text{ W kg}^{-1}$  is observed at the specific energy of  $26.9 \text{ W h kg}^{-1}$  (Fig. 5h). Such high output energy and power densities of the hybrid device (details are listed in Table S4) greatly outperform those of the recently reported  $\text{Ni(OH)}_2$ -based hybrid devices, including  $\beta\text{-Ni(OH)}_2//\text{AC}$  [12],  $\text{Ni(OH)}_2/\text{AC}/\text{CNT}/\text{AC}$  [58],  $\text{CNT}/\text{Ni(OH)}_2//\text{AC}$  [8],  $\text{Ni(OH)}_2/\text{graphite}/\text{AC}$  [27],  $\text{rGO}/\text{Ni(OH)}_2//\text{AC}$  [59], and  $\text{Ni(OH)}_2/\text{CVD graphene}/\text{AC}$  [60]. These results suggest that  $\text{Ni(OH)}_2/\text{G}/\text{Ni(OH)}_2/\text{NF}$  integrated electrode is promising candidate for supercapacitor with high energy and power densities. To further investigate the self-discharge behavior, the supercapacitor device was charged to 1.5 V at the current density of  $1 \text{ A g}^{-1}$ , kept at 1.5 V for 2 h, and then the open-circuit potential was measured as a function of time. Fig. S15 shows the OCV of the ASC device undergoes fast decay in the initial around 3.5 h, and remains to 1.04 V within 12 h, indicating a sustained self-discharging performance, which is a vital requirement for practical application of supercapacitors.

#### 4 Conclusions

In summary, we have designed integrated electrode architecture of  $\text{Ni(OH)}_2/\text{G}/\text{Ni(OH)}_2/\text{NF}$  for supercapacitors. The resulting  $\text{Ni(OH)}_2/\text{G}/\text{Ni(OH)}_2/\text{NF}$

electrode is endowed with good electric conductivity and structural robustness, providing rapid and efficient pathways for fast electron transport; thus, it exhibits an ultrahigh specific capacity of  $991 \text{ C g}^{-1}$  at a current density of  $1 \text{ A g}^{-1}$ , good rate capability of 70.7% at  $20 \text{ A g}^{-1}$ , and outstanding cycling performance retaining approximately 95.4% of its initial capacity after 5000 cycles. More importantly, a hybrid supercapacitor assembled from  $\text{Ni(OH)}_2/\text{G}/\text{Ni(OH)}_2/\text{NF}$  and  $\text{AC}/\text{NF}$  delivers a high specific energy of  $49.5 \text{ W h kg}^{-1}$  at a power density of  $750 \text{ W kg}^{-1}$ . Furthermore, the hybrid device exhibits the high power density of  $7500 \text{ W h kg}^{-1}$  at the specific density of  $26.9 \text{ W kg}^{-1}$  with an excellent cycling lifespan.

### **Acknowledgements**

This research was partially supported by Nanomaterial Technology Development Program (NRF-2017M3A7B4041987), the Korean Government (MSIP) (No. 2015R1A5A1037668) and the Science and Technology Development Fund of the Macau SAR (FDCT-098/2015/A3).

### **Conflicts of interest**

The authors declare there are no conflicts of interest.

## Figures

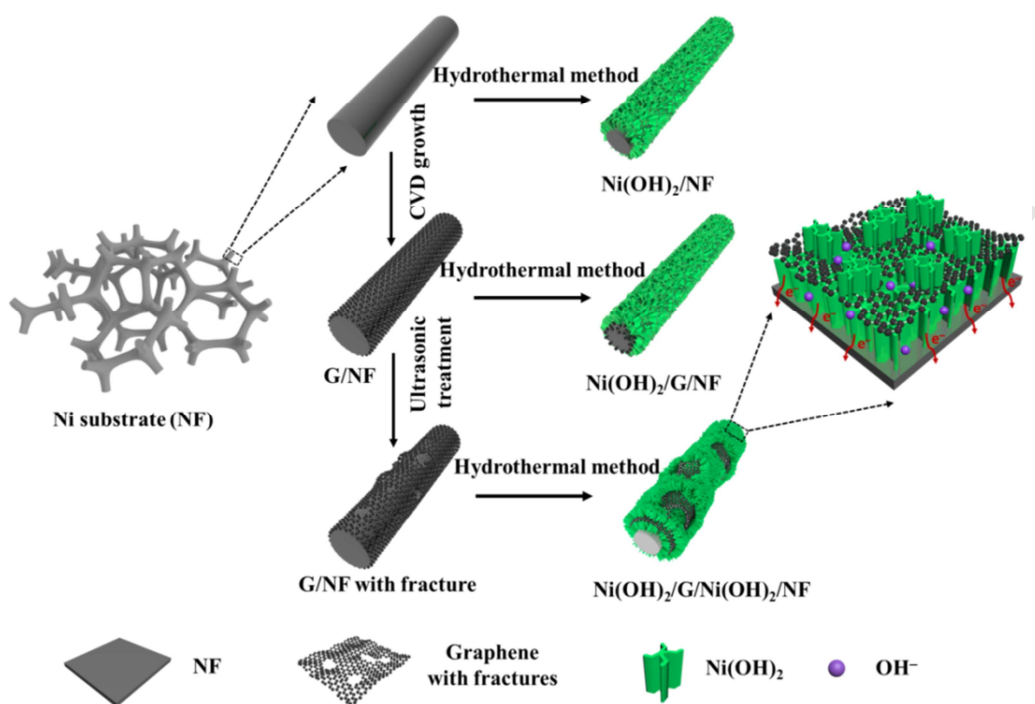


**Fig. 1** Schematic illustration for the fabrication of the Ni(OH)<sub>2</sub>/NF, Ni(OH)<sub>2</sub>/G/NF, and Ni(OH)<sub>2</sub>/G/Ni(OH)<sub>2</sub>/NF integrated architectures.

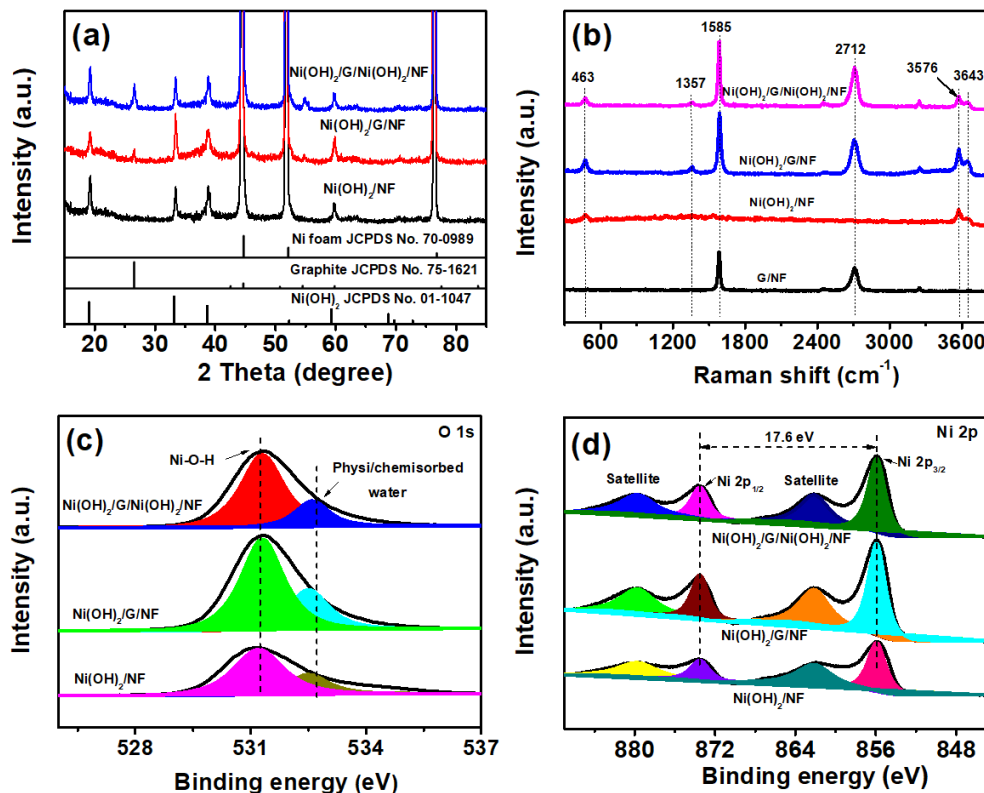


**Fig. 2** (a) XRD patterns of the  $\text{Ni(OH)}_2/\text{NF}$ ,  $\text{Ni(OH)}_2/\text{G/NF}$ , and  $\text{Ni(OH)}_2/\text{G/Ni(OH)}_2/\text{NF}$ . (b) Raman spectra of  $\text{G/NF}$ ,  $\text{Ni(OH)}_2/\text{NF}$ ,  $\text{Ni(OH)}_2/\text{G/NF}$ , and  $\text{Ni(OH)}_2/\text{G/Ni(OH)}_2/\text{NF}$ . High-resolution XPS spectra of (c) O 1s and (d) Ni 2p for  $\text{G/NF}$ ,  $\text{Ni(OH)}_2/\text{NF}$ ,  $\text{Ni(OH)}_2/\text{G/NF}$ , and  $\text{Ni(OH)}_2/\text{G/Ni(OH)}_2/\text{NF}$ .

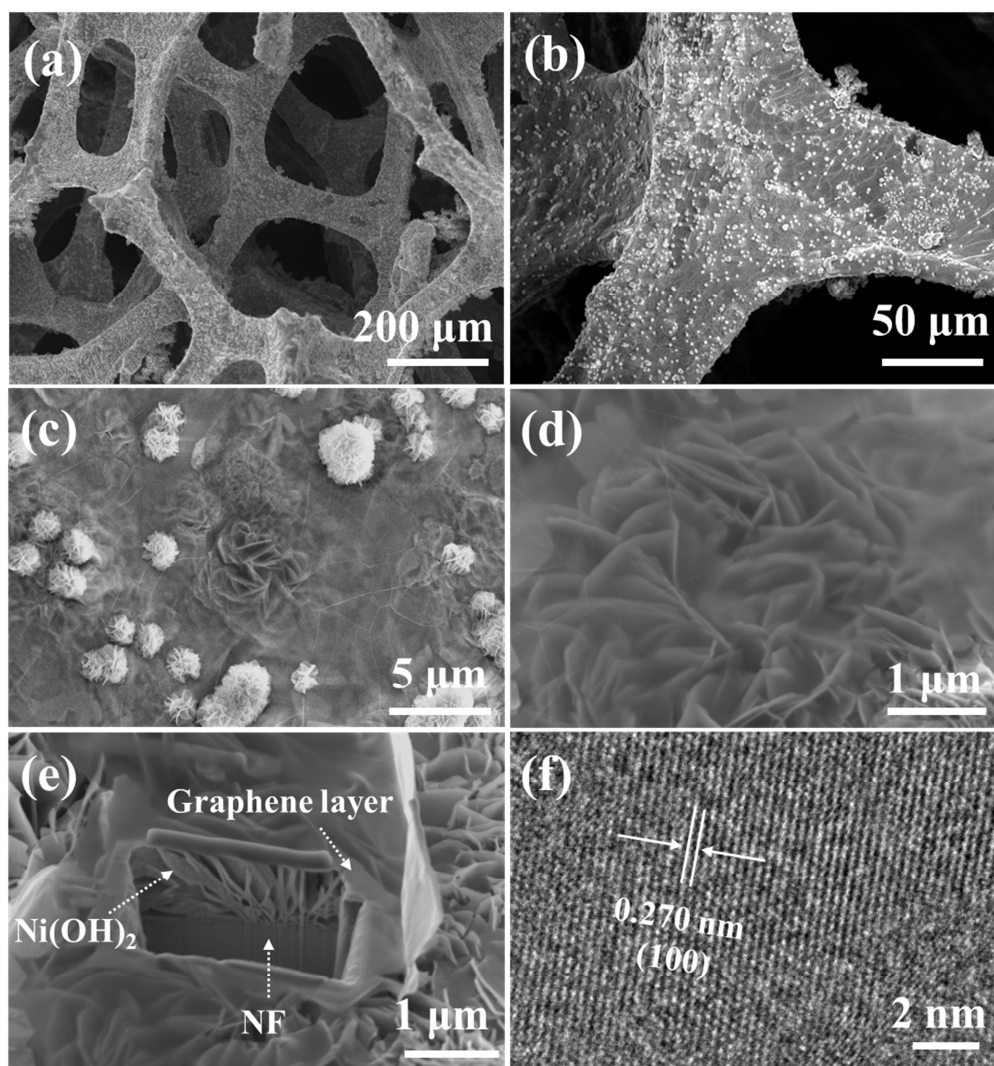


**Fig. 3** (a-d) Typical SEM images of Ni(OH)<sub>2</sub>/G/Ni(OH)<sub>2</sub>/NF at different magnifications. (e) SEM image of a micrometer-scale region of a micromachined specimen by FIB milling. (f) TEM image of the FIB-ablated area of the embedded Ni(OH)<sub>2</sub>.

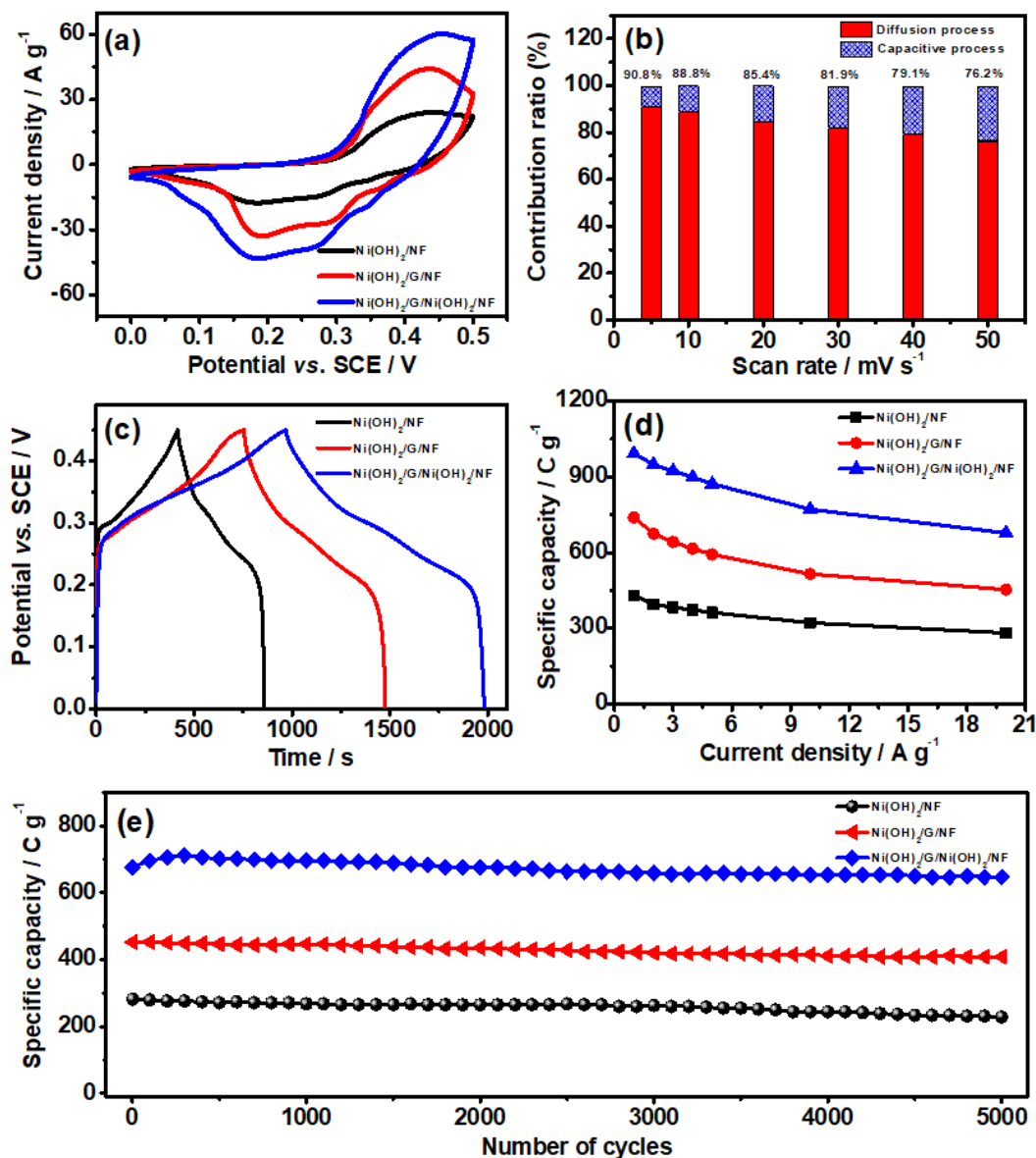


**Fig. 4** Electrochemical characterization of the Ni(OH)<sub>2</sub>/NF, Ni(OH)<sub>2</sub>/G/NF, and Ni(OH)<sub>2</sub>/G/Ni(OH)<sub>2</sub>/NF electrodes: (a) CV curves at a scan rate of 30 mV s<sup>-1</sup>. (b) Contribution ratio of faradaic diffusion-controlled and capacitive charge storage for Ni(OH)<sub>2</sub>/G/Ni(OH)<sub>2</sub>/NF electrode at different scan rates. (c) GCD curves at a current density of 1 A g<sup>-1</sup>. (d) Comparison of the specific capacity as a function of the current density. (e) Cycling stability at a current density of 20 A g<sup>-1</sup>.

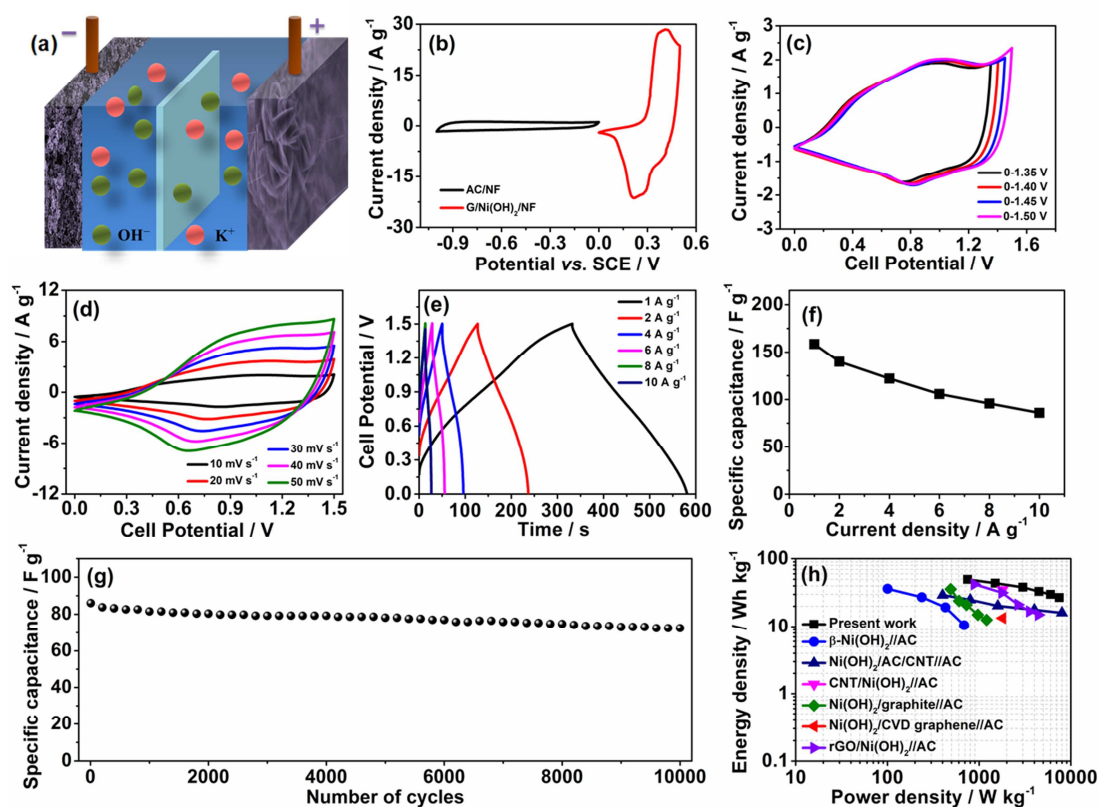


**Fig. 5** Electrochemical performance of the assembled hybrid supercapacitor: (a) schematic illustration of the assembled hybrid device, (b) CV curves collected for AC/NF and Ni(OH)<sub>2</sub>/G/Ni(OH)<sub>2</sub>/NF electrodes at a scan rate of 5 mV s<sup>-1</sup>, (c) CV curves in different cell potentials, (d) CV curves at different scan rates, (e) GCD curves at different current densities, (f) specific capacitance at different current densities, (g) cycling performance at a current density of 10 A g<sup>-1</sup>, and (h) Ragone plot comparison with other hybrid devices employing Ni(OH)<sub>2</sub>-based materials from the literature.

## References

- [1] J. Zhao, Y. Jiang, H. Fan, M. Liu, O. Zhuo, X. Wang, Q. Wu, L. Yang, Y. Ma, Z. Hu, Porous 3D Few-Layer Graphene-like Carbon for Ultrahigh-Power Supercapacitors with Well-Defined Structure-Performance Relationship, *Adv. Mater.*, 29 (2017) 1604569.
- [2] N. Bagheri, A. Aghaei, N. Vlachopoulos, M. Skunik-Nuckowska, P.J. Kulesza, L. Häggman, G. Boschloo, A. Hagfeldt, Physicochemical identity and charge storage properties of battery-type nickel oxide material and its composites with activated carbon, *Electrochim. Acta*, 194 (2016) 480-488.
- [3] J. Zhu, D. Song, T. Pu, J. Li, B. Huang, W. Wang, C. Zhao, L. Xie, L. Chen, Two-dimensional porous  $\text{ZnCo}_2\text{O}_4$  thin sheets assembled by 3D nanoflake array with enhanced performance for aqueous asymmetric supercapacitor, *Chem. Eng. J.*, 336 (2018) 679-689.
- [4] F.-X. Ma, L. Yu, C.-Y. Xu, X.W.D. Lou, Self-supported formation of hierarchical  $\text{NiCo}_2\text{O}_4$  tetragonal microtubes with enhanced electrochemical properties, *Energy Environ. Sci.*, 9 (2016) 862-866.
- [5] S. Liu, S.C. Jun, Hierarchical manganese cobalt sulfide core-shell nanostructures for high-performance asymmetric supercapacitors, *J. Power Sources*, 342 (2017) 629-637.
- [6] S. Liu, S.C. Lee, U. Patil, I. Shackery, S. Kang, K. Zhang, J.H. Park, K.Y. Chung, S.C. Jun, Hierarchical MnCo-layered double hydroxides@ $\text{Ni}(\text{OH})_2$  core-shell heterostructures as advanced electrodes for supercapacitors, *J. Mater. Chem. A*, 5 (2017) 1043-1049.
- [7] H. Wang, J. Yan, R. Wang, S. Li, D.J. Brett, J. Key, S. Ji, Toward high practical capacitance of  $\text{Ni}(\text{OH})_2$  using highly conductive CoB nanochain supports, *J. Mater. Chem. A*, 5 (2017) 92-96.
- [8] R.R. Salunkhe, J. Lin, V. Malgras, S.X. Dou, J.H. Kim, Y. Yamauchi, Large-scale synthesis of coaxial carbon nanotube/ $\text{Ni}(\text{OH})_2$  composites for asymmetric supercapacitor application, *Nano Energy*, 11 (2015) 211-218.
- [9] S. Liu, S.C. Lee, U.M. Patil, C. Ray, K.V. Sankar, A. Kundu, S. Kang, J.H. Park, S.C. Jun, Controllable Sulfuration Engineered NiO Nanosheets with Enhanced Capacitance for High Rate Supercapacitors, *J. Mater. Chem. A*, 5 (2017) 4543-4549.
- [10] L. Xuan, L. Chen, Q. Yang, W. Chen, X. Hou, Y. Jiang, Q. Zhang, Y. Yuan, Engineering 2D multi-layer graphene-like  $\text{Co}_3\text{O}_4$  thin sheets with vertically aligned nanosheets as basic building units for advanced pseudocapacitor materials, *J. Mater. Chem. A*, 3 (2015) 17525-17533.

- [11] J. Yan, W. Sun, T. Wei, Q. Zhang, Z. Fan, F. Wei, Fabrication and electrochemical performances of hierarchical porous Ni(OH)<sub>2</sub> nanoflakes anchored on graphene sheets, *J. Mater. Chem.*, 22 (2012) 11494-11502.
- [12] J. Huang, P. Xu, D. Cao, X. Zhou, S. Yang, Y. Li, G. Wang, Asymmetric supercapacitors based on  $\beta$ -Ni(OH)<sub>2</sub> nanosheets and activated carbon with high energy density, *J. Power Sources*, 246 (2014) 371-376.
- [13] S. Zhao, R. Jin, H. Abroshan, C. Zeng, H. Zhang, S.D. House, E. Gottlieb, H.J. Kim, J.C. Yang, R. Jin, Gold Nanoclusters Promote Electrocatalytic Water Oxidation at the Nanocluster/CoSe<sub>2</sub> Interface, *J. Am. Chem. Soc.*, 139 (2017) 1077-1080.
- [14] B. Kiraly, R.M. Jacobberger, A.J. Mannix, G.P. Campbell, M.J. Bedzyk, M.S. Arnold, M.C. Hersam, N.P. Guisinger, Electronic and mechanical properties of graphene–germanium interfaces grown by chemical vapor deposition, *Nano Lett.*, 15 (2015) 7414-7420.
- [15] Z. Chen, W. Ren, L. Gao, B. Liu, S. Pei, H.-M. Cheng, Three-dimensional flexible and conductive interconnected graphene networks grown by chemical vapour deposition, *Nat Mater.*, 10 (2011) 424-428.
- [16] S.C. O'Hern, C.A. Stewart, M.S. Boutilier, J.-C. Idrobo, S. Bhaviripudi, S.K. Das, J. Kong, T. Laoui, M. Atieh, R. Karnik, Selective molecular transport through intrinsic defects in a single layer of CVD graphene, *ACS nano*, 6 (2012) 10130-10138.
- [17] P. Gupta, P.D. Dongare, S. Grover, S. Dubey, H. Mamgain, A. Bhattacharya, M.M. Deshmukh, A facile process for soak-and-peel delamination of CVD graphene from substrates using water, *Sci. Rep.*, 4 (2014), 3882.
- [18] P. Ramadass, B. Haran, R. White, B.N. Popov, Mathematical modeling of the capacity fade of Li-ion cells, *J. Power Sources*, 123 (2003) 230-240.
- [19] J. Xia, F. Chen, J. Li, N. Tao, Measurement of the quantum capacitance of graphene, *Nat. Nanotech.*, 4 (2009) 505.
- [20] S. Liu, K.H. Kim, J.M. Yun, A. Kundu, K.V. Sankar, U.M. Patil, C. Ray, S.C. Jun, 3D yolk–shell NiGa<sub>2</sub>S<sub>4</sub> microspheres confined with nanosheets for high performance supercapacitors, *J. Mater. Chem. A*, 5 (2017) 6292-6298.
- [21] S. Liu, K. San Hui, K.N. Hui, J.M. Yun, K.H. Kim, Vertically stacked bilayer CuCo<sub>2</sub>O<sub>4</sub>/MnCo<sub>2</sub>O<sub>4</sub> heterostructures on functionalized graphite paper for high-performance electrochemical capacitors., *J. Mater. Chem. A*, 4 (2016) 8061-8071.
- [22] Y. Zhao, L. Hu, S. Zhao, L. Wu, Preparation of MnCo<sub>2</sub>O<sub>4</sub>@ Ni(OH)<sub>2</sub> Core–Shell Flowers for Asymmetric Supercapacitor Materials with Ultrahigh Specific Capacitance, *Adv. Funct. Mater.*, 26 (2016) 4085-4093.

- [23] Q. Ren, R. Wang, H. Wang, J. Key, D.J. Brett, S. Ji, S. Yin, P.K. Shen, Ranunculus flower-like  $\text{Ni}(\text{OH})_2@ \text{Mn}_2\text{O}_3$  as a high specific capacitance cathode material for alkaline supercapacitors, *J. Mater. Chem. A*, 4 (2016) 7591-7595.
- [24] J. Lin, H. Jia, H. Liang, S. Chen, Y. Cai, J. Qi, C. Qu, J. Cao, W. Fei, J. Feng, In Situ Synthesis of Vertical Standing Nanosized NiO Encapsulated in Graphene as Electrodes for High-Performance Supercapacitors, *Adv. Sci.*, 5 (2018) 1700687.
- [25] X. Xiong, D. Ding, D. Chen, G. Waller, Y. Bu, Z. Wang, M. Liu, Three-dimensional ultrathin  $\text{Ni}(\text{OH})_2$  nanosheets grown on nickel foam for high-performance supercapacitors, *Nano Energy*, 11 (2015) 154-161.
- [26] Y.-Z. Su, K. Xiao, N. Li, Z.-Q. Liu, S.-Z. Qiao, Amorphous  $\text{Ni}(\text{OH})_2@$ three-dimensional Ni core-shell nanostructures for high capacitance pseudocapacitors and asymmetric supercapacitors, *J. Mater. Chem. A*, 2 (2014) 13845-13853.
- [27] H. Li, M. Yu, F. Wang, P. Liu, Y. Liang, J. Xiao, C. Wang, Y. Tong, G. Yang, Amorphous nickel hydroxide nanospheres with ultrahigh capacitance and energy density as electrochemical pseudocapacitor materials, *Nat. Commun.*, 4 (2013) 1894.
- [28] Y. Luo, J. Jiang, W. Zhou, H. Yang, J. Luo, X. Qi, H. Zhang, Y. Denis, C.M. Li, T. Yu, Self-assembly of well-ordered whisker-like manganese oxide arrays on carbon fiber paper and its application as electrode material for supercapacitors, *J. Mater. Chem.*, 22 (2012) 8634-8640.
- [29] Liu, S.; San Hui, K.; Hui, K. N.; Li, H.-F.; Ng, K. W.; Xu, J.; Tang, Z.; Jun, S. C., An asymmetric supercapacitor with excellent cycling performance realized by hierarchical porous  $\text{NiGa}_2\text{O}_4$  nanosheets, *J. Mater. Chem. A*, 5 (2017) 19046-19053.
- [30] K. Fan, H. Chen, Y. Ji, H. Huang, P.M. Claesson, Q. Daniel, B. Philippe, H. Rensmo, F. Li, Y. Luo, Nickel-vanadium monolayer double hydroxide for efficient electrochemical water oxidation, *Nat. Commun.*, 7 (2016) 11981.
- [31] J. Yan, Z. Fan, W. Sun, G. Ning, T. Wei, Q. Zhang, R. Zhang, L. Zhi, F. Wei, Advanced asymmetric supercapacitors based on  $\text{Ni}(\text{OH})_2/\text{graphene}$  and porous graphene electrodes with high energy density, *Adv. Funct. Mater.*, 22 (2012) 2632-2641.
- [32] P.V. Kamath, M. Ahmed, *J. Appl. Electrochem*, Cyclic voltammetric studies of nickel hydroxide and cobalt hydroxide thin films in alkali and alkaline earth metal hydroxides, 23 (1993) 225-230.
- [33] W. Xu, Z. Jiang, Q. Yang, W. Huo, M.S. Javed, Y. Li, L. Huang, X. Gu, C. Hu, Approaching the lithium-manganese oxides' energy storage limit with  $\text{Li}_2\text{MnO}_3$  nanorods for high-performance supercapacitor, *Nano Energy*, 43 (2018) 168-176.
- [34] L. Hou, Y. Shi, S. Zhu, M. Rehan, G. Pang, X. Zhang, C. Yuan, Hollow mesoporous hetero- $\text{NiCo}_2\text{S}_4/\text{Co}_9\text{S}_8$  submicro-spindles: unusual formation and

- excellent pseudocapacitance towards hybrid supercapacitors, *J. Mater. Chem. A*, 5 (2017) 133-144.
- [35] C.-C. Hu, J.-C. Chen, K.-H. Chang, Cathodic deposition of Ni(OH)<sub>2</sub> and Co(OH)<sub>2</sub> for asymmetric supercapacitors: importance of the electrochemical reversibility of redox couples, *J. Power Sources*, 221 (2013) 128-133.
- [36] S. Liu, Y. Yin, K.S. Hui, K.N. Hui, S.C. Lee, S.C. Jun, High-Performance Flexible Quasi-Solid-State Supercapacitors Realized by Molybdenum Dioxide@ Nitrogen-Doped Carbon and Copper Cobalt Sulfide Tubular Nanostructures, *Adv. Sci.*, 5 (2018) 1800733.
- [37] G. Meng, Q. Yang, X. Wu, P. Wan, Y. Li, X. Lei, X. Sun, J. Liu, Hierarchical mesoporous NiO nanoarrays with ultrahigh capacitance for aqueous hybrid supercapacitor, *Nano Energy*, 30 (2016) 831-839.
- [38] L.L. Zhang, X. Zhao, H. Ji, M.D. Stoller, L. Lai, S. Murali, S. McDonnell, B. Cleveger, R.M. Wallace, R.S. Ruoff, Nitrogen doping of graphene and its effect on quantum capacitance, and a new insight on the enhanced capacitance of N-doped carbon, *Energy Environ. Sci.*, 5 (2012) 9618-9625.
- [39] H. Yi, H. Wang, Y. Jing, T. Peng, Y. Wang, J. Guo, Q. He, Z. Guo, X. Wang, Advanced asymmetric supercapacitors based on CNT@Ni(OH)<sub>2</sub> core-shell composites and 3D graphene networks, *J. Mater. Chem. A*, 3 (2015) 19545-19555.
- [40] X. Wang, Y. Wang, C. Zhao, Y. Zhao, B. Yan, W. Zheng, Electrodeposited Ni(OH)<sub>2</sub> nanoflakes on graphite nanosheets prepared by plasma-enhanced chemical vapor deposition for supercapacitor electrode, *New J. Chem.*, 36 (2012) 1902-1906.
- [41] S. Min, C. Zhao, G. Chen, X. Qian, One-pot hydrothermal synthesis of reduced graphene oxide/Ni(OH)<sub>2</sub> films on nickel foam for high performance supercapacitors, *Electrochim. Acta*, 115 (2014) 155-164.
- [42] S. Min, C. Zhao, Z. Zhang, G. Chen, X. Qian, Z. Guo, Synthesis of Ni(OH)<sub>2</sub>/RGO pseudocomposite on nickel foam for supercapacitors with superior performance, *J. Mater. Chem. A*, 3 (2015) 3641-3650.
- [43] Y. Xu, X. Huang, Z. Lin, X. Zhong, Y. Huang, X. Duan, One-step strategy to graphene/Ni(OH)<sub>2</sub> composite hydrogels as advanced three-dimensional supercapacitor electrode materials, *Nano research*, 6 (2013) 65-76.
- [44] J. Shen, J. Wu, L. Pei, M.T.F. Rodrigues, Z. Zhang, F. Zhang, X. Zhang, P.M. Ajayan, M. Ye, CoNi<sub>2</sub>S<sub>4</sub>-Graphene-2D-MoSe<sub>2</sub> as an Advanced Electrode Material for Supercapacitors, *Adv. Energy Mater.*, 6 (2016) 1600341.
- [45] X.a. Chen, X. Chen, F. Zhang, Z. Yang, S. Huang, One-pot hydrothermal synthesis of reduced graphene oxide/carbon nanotube/ $\alpha$ -Ni(OH)<sub>2</sub> composites for high performance electrochemical supercapacitor, *J. Power Sources*, 243 (2013) 555-561.

- [46] Y. Liu, G. Yuan, Z. Jiang, Z. Yao, M. Yue, Preparation of Ni(OH)<sub>2</sub>-graphene sheet-carbon nanotube composite as electrode material for supercapacitors, *J. Alloys Compd.*, 618 (2015) 37-43.
- [47] J. Zhang, S. Liu, G. Pan, G. Li, X. Gao, A 3D hierarchical porous  $\alpha$ -Ni(OH)<sub>2</sub>/graphite nanosheet composite as an electrode material for supercapacitors, *J. Mater. Chem. A*, 2 (2014) 1524-1529.
- [48] S. Kandula, K.R. Shrestha, N.H. Kim, J.H. Lee, Fabrication of a 3D Hierarchical Sandwich Co<sub>9</sub>S<sub>8</sub>/ $\alpha$ -MnS@N-C@MoS<sub>2</sub> Nanowire Architectures as Advanced Electrode Material for High Performance Hybrid Supercapacitors, *Small*, 14 (2018) 1800291.
- [49] S. Liu, Y. Yin, K.S. Hui, K.N. Hui, S.C. Lee, S.C. Jun, High Performance Flexible Quasi-Solid-State Supercapacitors Realized by Molybdenum Dioxide@Nitrogen-Doped Carbon and Copper Cobalt Sulfide Tubular Nanostructures, *Adv. Sci.*, 5 (2018) 1800733.
- [50] S. Cruz-Manzo, P. Rama, R. Chen, The Low Current Electrochemical Mechanisms of the Fuel Cell Cathode Catalyst Layer Through an Impedance Study, *J. Electrochem. Soc.*, 157 (2010) B400-B408.
- [51] J.-B. Jorcin, M.E. Orazem, N. Pébère, B. Tribollet, CPE analysis by local electrochemical impedance spectroscopy, *Electrochim. Acta*, 51 (2006) 1473-1479.
- [52] P. Córdoba-Torres, T. Mesquita, O. Devos, B. Tribollet, V. Roche, R. Nogueira, On the intrinsic coupling between constant-phase element parameters  $\alpha$  and  $Q$  in electrochemical impedance spectroscopy, *Electrochim. Acta*, 72 (2012) 172-178.
- [53] W.-C. Chen, T.-C. Wen, Electrochemical and capacitive properties of polyaniline-implanted porous carbon electrode for supercapacitors, *J. Power Sources*, 117 (2003) 273-282.
- [54] C. Lei, F. Markoulidis, Z. Ashitaka, C. Lekakou, Reduction of porous carbon/Al contact resistance for an electric double-layer capacitor (EDLC), *Electrochim. Acta*, 92 (2013) 183-187.
- [55] W. Mulder, J. Sluyters, T. Pajkossy, L. Nyikos, Tafel current at fractal electrodes: connection with admittance spectra, *J Electroanal Chem Interfacial Electrochem*, 285 (1990) 103-115.
- [56] S. Liu, D. Ni, H.-F. Li, K.N. Hui, C.-Y. Ouyang, S.C. Jun, 1. Liu, S.; Ni, D.; Li, H.-F.; Hui, K. N.; Ouyang, C.-Y.; Jun, S. C., Effect of cation substitution on the pseudocapacitive performance of spinel cobaltite MCo<sub>2</sub>O<sub>4</sub> (M= Mn, Ni, Cu, and Co), *J. Mater. Chem. A*, 6 (2018) 10674-10685.
- [57] Y.Z. Zhang, T. Cheng, Y. Wang, W.Y. Lai, H. Pang, W. Huang, A Simple Approach to Boost Capacitance: Flexible Supercapacitors Based on Manganese Oxides@MOFs via Chemically Induced In Situ Self-Transformation, *Adv. Mater.*, 28 (2016) 5242-5248.

- [58] L. Sui, S. Tang, Y. Chen, Z. Dai, H. Huangfu, Z. Zhu, X. Qin, Y. Deng, G.M. Haarberg, An asymmetric supercapacitor with good electrochemical performances based on Ni(OH)<sub>2</sub>/AC/CNT and AC, *Electrochim. Acta*, 182 (2015) 1159-1165.
- [59] H. Yan, J. Bai, B. Wang, L. Yu, L. Zhao, J. Wang, Q. Liu, J. Liu, Z. Li, Electrochemical reduction approach-based 3D graphene/Ni(OH)<sub>2</sub> electrode for high-performance supercapacitors, *Electrochim. Acta*, 154 (2015) 9-16.
- [60] J. Ji, L.L. Zhang, H. Ji, Y. Li, X. Zhao, X. Bai, X. Fan, F. Zhang, R.S. Ruoff, Nanoporous Ni(OH)<sub>2</sub> thin film on 3D ultrathin-graphite foam for asymmetric supercapacitor, *ACS nano*, 7 (2013) 6237-6243.